Ageing of electrochemical double layer capacitors

A.M. Bittner [a,b,c,*], M. Zhu [c,d], Y. Yang [c,e], H.F. Waibel [c], M. Konuma [c], U. Starke [c], C.J. Weber [f]

a CIC nanoGUNE Consolider, Tolosa Hiribidea 76, E-20018 Donostia, Spain
b Ikerbasque, Basque Foundation for Science, E-48011 Bilbao, Spain
c Max-Planck-Institute for Solid State Research, Heisenbergstr. 1, D-70569 Stuttgart, Germany
d Merck China, Chemical Technology Office, Shanghai, PR China
e Department of Chemistry and Geochemistry, Colorado School of Mines, Golden, USA
f Freudenberg Vliesstoffe KG, Weinheim, Germany

ARTICLE INFO

ABSTRACT

The activated carbon in electrochemical double layer electrodes undergoes slow ageing. The effect becomes only apparent when capacitors are polarized to voltages at or above specified limits, or at high temperatures, for at least several months. A combination of "post mortem" analysis methods shows that the pores in the carbon are modified structurally, mainly by clogging up with organic species, but also electrochemically by decomposition of electrolyte, and by reduction and oxidation of the carbon in the electrodes. Key chemicals are trace water, the solvent acetonitrile, and the salt tetraethyl ammonium tetrafluoroborate. The changes differ hugely between negative and positive pole; the positively polarized electrode is much more affected. Also other compounds of the device, e.g. aluminum electrode support and paper separator, exhibit chemical ageing.

1. Introduction

1.1. Electrochemical double layer capacitors (EDLCs)

EDLCs are based on the purely electrostatic principle of accumulation of ions close to surfaces (electrodes) in a liquid solvent. Cations of an electrolyte salt accumulate at the negatively charged surface (hereinafter "cathode", which is electrochemically correct only during charging), and anions at the positively charged "anode". Both electrodes are highly porous to achieve a high surface to mass (or volume) ratio, but the details of pore size and pore volume can be as important as the surface area. The process of charging is nearly reversible; consequently, EDLCs are expected to have a much longer cycle life than batteries. While charge–discharge cycles in batteries are usually slow (due to the electrochemical processes), charging the EDL is very fast, even in porous electrodes. Such rapid cycles (technical range: seconds) allow for devices with high specific power, which can be an ideal add-on to devices of high specific energy (batteries or fuel cells) [1]. EDLCs and EDLC modules can be used in portable electric devices, hybrid electric vehicles, passenger cars, buses and even locomotives. In low-power portable devices, EDLCs can sustain low drain-rate memories, microprocessors, and real time clocks [2]. Higher powers are used for engine start and acceleration, and for regenerative braking [3]. Other important application areas are devices that cannot be connected to conventional power supplies, e.g. windmills or short stretches of tram lines [3].

Especially for widespread use in huge numbers, low-cost manufacturing is required, and simple designs based on cheap materials are necessary. At the same time, volume and mass should be kept small. A standard setup has emerged over the last decade: aluminum contact foils, coated on both sides with activated carbon (AC) [4], an organic electrolyte, and a separator (e.g. paper). We here focus on tetraethyl ammonium tetrafluoroborate (TEA$^+$ TFB$^-$) in acetonitrile (AN), which has the advantage of high conductivity even at low temperatures. The electrodes are composed not only of AC, but contain a polymeric binder in order to allow facile coating of the aluminum foils, and a conductive additive, usually carbon black, to enhance electrical interconnections between AC particles. EDLCs can show a short "burn-in" phase where their electrical characteristics change considerably; however, this is very fast (hours to days). In contrast, slow ageing processes are of utmost importance since the devices are supposed to run for many years with nearly constant properties. High temperature or high voltage, or even reversal of polarity, can induce irreversible processes, such

as capacitance loss and performance deterioration, which are very slow (typical range: months) [1,4–14]. We carried out a detailed characterization of EDLCs, connected to a DC voltage over up to 15 months, supplemented by "post mortem" analysis by nitrogen porosimetry, Raman spectroscopy, elemental analysis, X-ray photoelectron spectroscopy (XPS), and infrared (IR) spectroscopy. In this way we determined ageing mechanisms for further improvement and development of EDLCs.

Many ageing processes are of physical nature, e.g. gas evolution and accumulation in closed systems increase the internal pressure, which in extreme cases causes structural destruction of EDLCs. These processes are tackled by improvements of the container, the venting system, etc. Here we focus on chemical mechanisms, which are of special relevance for long times. The prime targets are the electrolyte, whose ageing has been investigated in detail [9,13,14], and the electrodes, whose carbon is supposed to be electrochemically and structurally very stable. This is in fact true, but it is often overlooked that carbon is thermodynamically unstable with respect to oxidation and reduction. Especially in electrochemical systems, the redox chemistry of carbon can overcome kinetic barriers at very long time scales. We already characterized two electrode components, AC and conductive additives, in detail [15], carefully avoiding any complication of real systems, such as presence of aluminum [14], inhomogeneities, binder material. Here we include all materials by exclusively targeting complete capacitors of the type "ultracapacitor" (Epcos AG), sealed in aluminum casings. Ageing effects are expected to change the structural (physical) and chemical characteristics of the electrodes, the chemistry of the electrolyte [13,14], and – in extreme cases – even other components, and in this way the capacitance decreases, and the equivalent series resistance (ESR) increases. These two values can be employed to detect ageing quantitatively, even during use. We decided not to simulate actual temperature–current–voltage–time profiles close to applications, but to keep all values constant (a constant voltage translates into a constant near-zero current). We systematically varied temperature and voltage because a longterm use requires defined limits on their values.

1.2. Carbon materials in EDLCs

ACs can be obtained from a wide variety of carbonaceous materials. The cheapest and most frequently used on a commercial scale are peat, coal, brown coal, wood and coconut shell. However, it is not easy to control the extent and size distribution of resultant porosities when natural feedstocks are used, since they have large structural and chemical variability; even non-carbon atoms are present in sizeable amounts. Synthetic carbon-rich precursors (polymer resins) are purer, and result in reproducible pore size distributions. The basic structural element of AC is graphite with its sp^2 carbon, and indeed small graphitic units are present in AC. However, Byrne and Marsh [16] suggest sp^2 units arranged mainly in five-, six-, and seven-membered rings, and detailed models for AC have to incorporate also sp^3-bonded carbon atoms. Carbon black is electrically conductive and is widely applied for conductivity

improvement in polymer engineering and electrochemical industry. When carbon black particles of diameters in the 100 nm range are homogeneously dispersed and mixed with AC, agglomerates of the aggregates are formed, in which a compact one-, two- or three-dimensional network of the conducting phase is obtained, thereby increasing the conductivity. In the electrodes used in ultracaps, AC was blended with carbon black and with a fluoropolymer binder.

1.3. Other materials in EDLCs

A simple and cost-effective setup implies the use of various compounds that make the system much more complex than a porous carbon electrode in electrolyte. As mentioned above, the microparticle nature of the carbon(s) requires a binder, here a fluoropolymer, in order to spread it as paste on the aluminum foil current collectors. The adhesion to the aluminum is promoted by a glue, usually carboxymethylcellulose, which is only present at the aluminum/AC interface. Aluminum is also used for the casing, and all aluminum surfaces have a thin layer of oxide, which does not impede electrical conduction significantly. The separator in our case was made from paper, with its intrinsically high porosity.

2. Experimental

2.1. Electrical testing

100 μm thick AC electrodes were produced from activated carbon (particle size around 3 μm, but many particles well below 1 μm) mixed with carbon black and binder, coated on aluminum foils. These were assembled in dry atmosphere with paper separators into 200 F ultracapacitors, housed in aluminum casings, and filled with electrolyte under reduced pressure. The electrolyte was tetraethyl ammonium tetrafluoroborate (TEA^+ TFB^-) in acetonitrile at a concentration of $\approx$1 M (mol l^{-1}) (battery grade). The technical specifications were as follows: mass 65 g, volume 56 ml, rated voltage 2.5 V, capacity 140 mAh (504 C), energy 625 J at 2.5 V, specific power 3.3 kW kg^{-1} and 3.9 kW l^{-1}, ESR max. 3.5 mΩ (DC), operating temperature −30 °C to 70 °C, cycle life time 500,000. The ultracapacitors were then polarized at various constant voltages, under various temperature conditions (Table 1), which define our ageing conditions I to VI. About every 600 h, capacitance and equivalent series resistance (ESR) were measured by electrochemical impedance spectroscopy with a PGSTAT30-FRA2 electrochemical analyzer (Autolab) in the frequency range from f = 1 kHz to 10 mHz. The capacitance C was calculated from the imaginary part of the complex impedance Z, according to $C = 1/(2\pi f |Z''|)$. The value at 2.5 V, 25 °C, and 50 mHz was used. This part of work was completed at Epcos AG in Heidenheim.

2.2. Sample preparation

After ageing, the ultracapacitors were transferred to MPI-FKF in Stuttgart, and cut open in an argon-filled box. Our analysis conditions allowed, different from the fabrication, for a certain level of

Table 1
Ageing conditions of ultracapacitors. The ageing factor is calculated from Ref. [10].

Ultracap code	Potential/V	Temp./°C	Time/h	Potential excursion/V	Temperature excursion/K	Ageing factor	Condition
I	2.5	80	3048	0.2	55	$2^{7.5}$	Failure
II	2.3	80	3115	0	55	$2^{5.5}$	Failure
III	2.5	70	3700	0.2	45	$2^{6.5}$	Damaged
IV	2.8	50	2919	0.5	25	$2^{7.5}$	Working
V	2.3	70	2904	0	45	$2^{4.5}$	Working
VI	2.5	50	2924	0.2	25	$2^{4.5}$	Working
Reference	2.3	25	24	0	0	2^0	Working

oxygen and water (up to 100 ppm). Electrodes and other materials were cut into small pieces (≈0.5 cm sides). Normally samples were taken from the middle part of the electrodes. The samples were immersed into a large quantity (≈10 ml for each piece) of acetonitrile overnight to let the adsorbed salt diffuse out. Then the electrodes were rinsed with the solvent (≈10 ml for each piece) with shaking to remove the salt. From our results, the removal is practically complete (see below). In the following procedures, the electrodes were exposed to laboratory air for short times (see below). The samples were pre-dried at 60 °C and vacuum-dried at 80 °C under ≈10^{-3} mbar overnight, to remove the water completely.

2.3. Porosimetry

Porous materials were characterized by volumetric titration with nitrogen at 77 K at various equilibrium pressure values with an Autosorb-1MP porosimeter (Quantachrome). This involved admitting a certain quantity of gas, and measuring the volume remaining in the gas phase for each pressure value, which yields an isotherm. After weighing, pretreatment normally was outgassing under high vacuum for 24 h. The samples were then refilled with nitrogen, and their mass was determined again, in order to reduce the error from adsorbed water and air. This took only 2–5 min. Since the sample tube was too long for our balance, a small quartz tube of 3 mm diameter and 10 cm length was designed. Samples were first placed in the small tube and weighed, then both were placed in the Quantachrome 9 mm diameter tube for outgassing and measuring. The specific surface area of the samples was calculated with five-point BET in the range from P/P_0 = 0.01–0.1. Calculations with DR and DFT models were carried out with the software Autosorb (Quantachrome).

2.4. Raman spectroscopy

Raman spectra were obtained with a Labram 010 spectrometer (Jobin Yvon Horiba) at 632.8 nm excitation. Dried electrode samples were placed on microscope slides. The power was 4 mW, the spot size was adjusted in the range 10–40 μm. Spectra from 500 to 4000 cm^{-1} at ≈1 cm^{-1} intervals were recorded for 100 s in backscattering geometry with a single monochromator. The slit width was set to 100 μm, and 5 scans were averaged. The detector was an electrically cooled charge coupled device. The spectra were first calibrated by polynomial baseline subtraction with the Labram software, a process that proved to be well reproducible. A deconvolution was carried out in Origin 7.5 with five Lorentzian shape peaks on top of a linear background in the region from 800 to 2000 cm^{-1}. Beyssac et al. [17] reported that the structural heterogeneity of carbonaceous materials like natural coal, cokes and anthracite limit the applicability of Raman microspectroscopy for characterization. However, they also found that this shortcoming can be compensated by adopting large probing laser spots of ≈40 μm diameter. Since the largest particle size of our ACs was below 5 μm, the laser spot always probed several primary particles. Therefore the recorded spectra should be representative for the investigated samples.

2.5. Elemental analysis

Elemental analysis for carbon, hydrogen, and nitrogen was performed on a Perkin Elmer Analyzer 240 at the University of Stuttgart. The electrodes were stripped off from the aluminum foil, and cut into small pieces (less than 1 mm sides). The samples were rinsed and dried at 80 °C and ≈10^{-3} mbar. The samples were carefully sealed by in plastic foil to prevent interference from water, and the time between drying and measurement was minimized.

However, it still was several hours, much longer than for the other methods.

2.6. IR spectroscopy

Infrared spectra were collected on an Equinox 55 infrared spectrometer (Bruker, Germany) with a Globar mid infrared source and a deuterated triglycine sulfate detector. An attenuated total reflection configuration setup (PIKE Miracle) with a germanium crystal as the internal reflection element was used. The sample chamber was continuously purged with argon 5.0 (99.999 vol.%) at the rate of ≈4 l min^{-1} to reduce the interference of water and carbon dioxide. 2000 scans were added at a resolution of 8 cm^{-1}. Between two measurements, the crystal was cleaned with water, wiped with soft lens paper, and dried for 10 min. A micrometer screw with a flat end was placed on the samples to improve the contact to the crystal. The transmittance spectra were generated from raw spectra, referenced to the raw spectra of air. We additionally checked for contamination or inhomogeneity by exposing the inner part of the electrodes: the samples were stripped with adhesive tape, and analyzed layer by layer (approximately 30–40 μm per layer, estimated from the overall thickness of 100 μm). The spectra were very similar for all layers.

2.7. XPS

X-ray photoelectron spectra were recorded in an AXIS Ultra ESCA (Kratos Analytical Ltd., UK) with photoelectron excitation by monochromatized Al Kα radiation (1486.6 eV). The X-ray power was set to 150 W (15 kV, 10 mA). The base pressure in the sample analysis chamber was <10^{-9} mbar. Directly after drying, samples were transferred into the instrument. The spectra obtained indicated no interference from water, which would show a strong O1s signal at 535–536 eV. The samples were sputtered with an argon ion gun to remove the top 20 nm to prevent recording possible contamination, which normally occurs during sample preparation and sample loading. Indeed the spectra showed changes, especially for the content of elements in the first 10 nm. For 20 nm and more the analysis did not change [18]. The samples exhibited charging due to their large thickness and relatively low conductivity. This was counteracted with a neutralizer (a heated tungsten filament as electron emitter). All results are the average from three measurements.

Analysis area on the sample surface was ≈0.3 mm × 0.7 mm. Survey spectra (1200 eV to −5 eV) were recorded with a pass energy of 80 eV, while the narrow scans for F1s, O1s, N1s, and C1s were recorded with a pass energy of 20 eV. Quantification was done by means of the relative elemental sensitivity factor method, which uses the sensitivity factors referenced to F1s, determined experimentally from compounds with defined stoichiometry. The curve fitting of C1s, N1s, O1s, and F1s envelopes was carried out with a mixed Gaussian (30%)–Lorentzian (70%) profile, after subtraction of a Shirley background with the CasaXPS processing software. The binding energy was calibrated with the C1s photoelectron peak from graphitic carbon at 284.6 eV.

3. Results and discussion

3.1. Impedance and mass changes of capacitors

The important parameters for supercapacitors are capacitance and ESR, which should be as high and as low as possible, respectively, and constant. However, the capacitance decreases, and the ESR increases slowly (Table 1, Fig. 1). While the capacitance in a modular setup can be increased by using additional EDLCs, the ESR increase translates into a loss of power, which cannot be compensated; it will even be aggravated in serial connections. It is
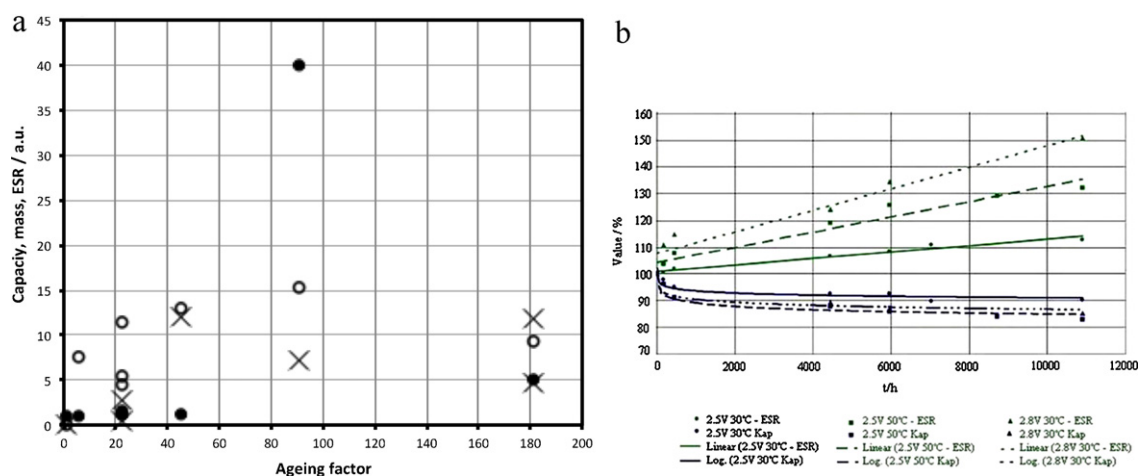
Fig. 1. (a) Loss of capacity in % (0 for fresh capacitor) (circles), relative ESR increase factor (1 for fresh capacitor) (disks), and mass loss of samples in % (0 for fresh capacitor) (crosses). Ageing conditions see Table 1. Horizontal axis: ageing factor according to Ref. [10]. (b) Capacitor ageing followed under various conditions of temperatures and voltages, for very long times. The increase/decrease % of ESR and capacitance are plotted. Linear (ESR) and logarithmic (capacitance) fits are shown.

known that voltage and temperature can both speed up this ageing [2,5–7,10,13], which is evident also in our data. The problem is that exactly these two quantities are very much searched for: high voltages are key for high powers, and high temperatures (e.g. when used in the vicinity of hot devices) have to be specified for certain application profiles.

An empirical rule based on propylene carbonate electrolyte states that an increase of 0.1 V or 10 K will each halve the lifetime [10]. Following this relationship, for our samples the order of ageing should be I = IV > III > II > V = VI (Table 1). However, samples I and II show increase of ESR and decrease of capacitance by several orders of magnitude, translating into total loss of performance. For the other samples, Fig. 1 shows that the mentioned order is, at least under severe conditions, not observed. On the one hand, the empirical rule is a rather rough estimate; on the other hand, the rule was not developed for AN with its low boiling point (82 °C). The buildup of internal pressure can be tackled (sealed DLCAP^{TM} capacitors from Nippon Chemi-Con are specified even up to 85 °C), but some EDLCs, including ultracaps, have mechanical pressure releases, which will speed up solvent evaporation at elevated temperatures. This can continue up to apparently complete dryness, as found in the "post mortem" analysis.

The mass loss resulting from the release can be followed and correlated with the other parameters (Fig. 1). As expected, the samples I and II, aged close to the boiling point of AN, show extreme loss. Solvent loss can cause precipitation of the TEA$^+$ TFB$^-$ salt, which removes mobile ions and clogs up pores. However, when the temperature is kept below extreme values, the influence from voltage increase can become more important than temperature increases (Fig. 1, sample pairs III and V at 70 °C, and IV and VI at 50 °C), as is always the case for completely sealed capacitors.

3.2. Structural ageing of the electrodes

3.2.1. Porosimetry

Theoretically, the specific area of the AC electrode is proportional to the double layer capacitance. However, the presence of small pores can change this to a surprising extent, for example by reduced accessibility of micropores to ions [19]. Qu and Shi [20] found that pore size distributions, determined from adsorption isotherms, can be taken as a guiding line. In practical terms, reproducibility is very important, so we collected data from two or three samples from each capacitor. The adsorption isotherms of the electrode were in some cases measured for both increasing and

decreasing pressures, but we detected negligible hysteresis effects (which would be characteristic for a large fraction of mesopores). Moreover, isotherms of electrodes aged at various conditions do not show significant differences in shape and adsorptive capacitance. Hence only the comparison between new electrodes (without any contact with the electrolyte or any other treatment) and aged electrodes are shown in Fig. 2. All isotherms are of type I, which means the electrodes keep their microporous structure after ageing. The measurement of a reference sample (polarized only for 24 h) shows no obvious decrease in specific area and pore volume in both anode and cathode, compared to the new electrode, which means the rinsing procedure (see Section 2) is effective. Furthermore, immersion/emersion, and even short term polarization have little effect on the pore structure.

We employ three models, Brunauer–Emmett–Teller (BET), Dubinin–Radushkevich (DR), and Density Functional Theory (DFT) to interpret the data. First, the BET model assumes that the uppermost molecules in adsorbed liquid layers are in equilibrium with the vapor. We used five values for relative pressures P/P_0 (P_0 is the vapor pressure) in the range from 0.01 to 0.1; at 0.1, pore filling is usually complete. Although the model is not strictly applicable in pores, the easily obtained surface area of porous solids is an important characterization parameter. In this case the obtained BET surface area does not reflect the true internal surface area, but
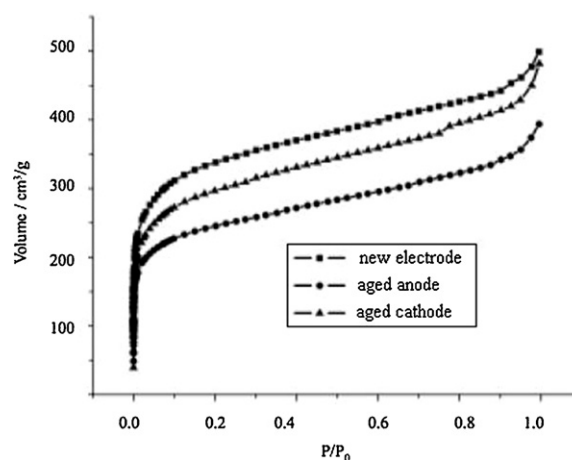

Fig. 2. Nitrogen adsorption isotherms (77 K) of new and aged electrodes. The sample mass comprises the active layer, not the aluminum part.

Table 2
Porosity characteristics of electrodes (specific areas and volumes).

Sample	S_{BET}/m^2 g^{-1}	S_{DR}/m^2 g^{-1}	V_{mic}/cm^3 g^{-1}	V_{total}/cm^3 g^{-1}
New electrode	1264	1297	0.46	0.59
I				
Anode	480	493	0.18	0.26
Cathode	1019	1043	0.37	0.48
II				
Anode	972	1043	0.37	0.44
Cathode	1140	1238	0.44	0.54
III				
Anode	911	962	0.35	0.43
Cathode	1115	1209	0.43	0.52
IV				
Anode	930	1019	0.36	0.43
Cathode	1141	1210	0.43	0.54
V				
Anode	910	976	0.35	0.42
Cathode	1127	1174	0.42	0.52
VI				
Anode	1061	1105	0.39	0.5
Cathode	1218	1240	0.44	0.59

should be considered as characteristic (or equivalent) BET area. In contrast, the DR model is based on adsorption energies that are very high for ultramicropores (0.4–0.7 nm), which can be assumed to be slit-shaped, as expected in AC. Pores of different size fill at different pressures, e.g. the "primary micropore filling" takes place at extremely low relative pressure P/P_0 (e.g. 0.001–0.01), and involves the entry of individual molecules into pores of 1–2 molecular diameters. Secondary micropore filling is cooperative, and occurs in micropores (2–5 molecular diameters). It involves adsorbate–adsorbate interactions (quasi-multilayer adsorption). The distribution of pore sizes is assumed to be Gaussian. Third, molecular models of adsorption such as DFT and Monte Carlo simulations give a much more accurate description of adsorption phenomena [21]. They are based on interaction model potentials such as the Lennard-Jones potential, and apply statistical mechanics to calculate sorbent properties at fixed temperature and pressure, by integrating over all individual pore properties. This requires fitting a pore size distribution to the experimental isotherm.

A detailed discussion can be based on our data listed in Table 2. We took the pore volume calculated by DFT as the total volume, and calculated the specific area (S_{BET}) with the BET method, and the volume (V_{mic}) and surface area (S_{mic}) of the micropores with the DR model. The porosity change (loss of pore volume, micropore volume, micropore specific area and BET specific area) is plotted versus the change of capacitance in Fig. 3(a) to give a clearer indication of the changes. Although the DR method and BET method give different absolute values for the specific area (BET underestimates the area, compared to DR), the ratios of the specific area loss for the aged samples, calculated with both methods, were similar. DFT gives much more reliable data, and we determined pore size distribution histograms for relative pressures P/P_0 from 7.7×10^{-6} to 0.7, corresponding to pore sizes from 0.5 to 5 nm (Fig. 3(b)). It is obvious that aged anodes suffer a higher pore volume loss and surface area loss than cathodes. The loss is comparable with results obtained for other types of porous carbon electrodes [5] and capacitors [6], which however withstand higher voltages at ambient temperature. Neither area nor volume loss can be quantitatively correlated with the capacitance. It is likely that a range of pores is blocked by ageing, but the data do not allow to point at a specific mechanism. In a certain range, between the more seriously aged sample II and the less aged sample VI, the pore characteristics were not very different. This hints that pore volume and specific area loss are only two of the many factors that affect EDLC ageing, as we will elucidate below

for chemical ageing. It is, however, worthwhile to investigate also pore size distributions.

The histograms in Fig. 3(b) show pore size distributions for ranges of pore sizes (0.5–0.63 nm, 0.63–0.79 nm, 0.79–1 nm, 1–1.26 nm, 1.26–1.58 nm, 1.58–2.0 nm, 2.0–2.5 nm, 2.5–3.2 nm, 3.2–4.0 nm, 4.0–5.0 nm). We consider such ranges more objective than the pore size distribution curve, which can be prone to artifacts, e.g. a minimum at ≈1 nm for a number of carbon materials. As mentioned above, one would expect a linear relationship of pore area (or relative porosity) with capacitance. We plot the capacitance (new EDLCs set to 100%) against the content of pores, for various pore size ranges, and for anodes and cathodes separately (Fig. 3(c)). The data show that, in anodes, pores with sizes in the ranges of 0.5–0.79 nm, 0.79–1.26 nm and 4–5 nm show no correlation with the capacitance, while the content of the pores with widths in the range of 1.26–3.2 nm can be correlated to the electrochemical capacitance quite well. In other words, ageing decreases the content of the pores in this size range. In cathodes, the amount of pores between 0.5 and 0.79 nm decreases with ageing, but much less than the decrease of the pores in the range of 1.26–3.2 nm for the anodes. The content of pores of larger than 1.26 nm does not change much with ageing. For pores from 0.79 to 1.26 nm, the relation of the pore content change and capacitance change follows no obvious rule.

The loss of pores in the size range of 1.26–3.2 nm for anodes can be interpreted as follows: sizes from 1.26 to 2 nm accommodate ions without solvation shell, while sizes from 2 nm to 3.2 nm are suitable for the solvated ions. As for smaller pores, the lack of correlation can be explained as follows: Kim et al. [22] found that a pore around two to three times larger than that of the electrolyte ions should be the most suitable pore size for a high capacitance; they calculated diameters of TEA$^+$ and TFB$^-$ to 0.74 nm and 0.49 nm, respectively, comparable with Ue's calculation of the molecular radii to 0.342 nm and 0.218 nm, respectively [23]. However, this does not necessarily allow for the required low ESR, since the ions require time for desolvation in such small pores. Endo et al. tried to take into account the solvation of propylene carbonate, and calculated solvated cation and anion diameters of 1.96 nm and 1.71 nm, respectively. Based on these results and on the assumption that the cation desolvation is the rate-limiting factor, they suggested that pore sizes between 1 and 2 nm are crucial and govern the capacitance of EDLCs [24]. Based on these assumptions, our observed loss of pores in 0.5–0.79 nm range in the cathodes should have little contribution to the capacitance loss. The loss of these pores can also be attributed to the pore blockage – at negative potentials, TEA$^+$ cations move into these pores and are blocked there because of the spatial confinement. Theoretically they can move out, but kinetically this process is very slow and this kind of blockage may accumulate gradually with ageing (technical operation is always facilitated by slow charging and fast discharging).

3.2.2. Raman spectroscopy

Raman spectra (excited at 633 nm) of all aged electrodes were very similar (Fig. 4), even between anodes and cathodes, so they are not very suitable to follow ageing. We detected no indication for binder, solvent, electrolyte, or glue [25]; each of the bands can be attributed to a vibrational mode of the ideal or disordered graphitic lattice. While for an ideal graphitic crystal only a few of these modes would be active, structural disorder can activate several otherwise forbidden ones, especially the D or "defect" bands (Table 3). We found no changes for the weak band at ≈2630 cm^{-1} (the D$_1$ overtone), and for ≈2922 cm^{-1} (the D$_1$ + G combination), but for the region below 2000 cm^{-1}. A detailed curve fitting (Fig. 4(b), Table 3) required five Lorentzians, which correspond to the bands D$_2$, G, D$_3$, D$_4$, and D$_1$, which we discuss in this order. First, the 1620 cm^{-1} band (D$_2$) can be observed as a shoulder on
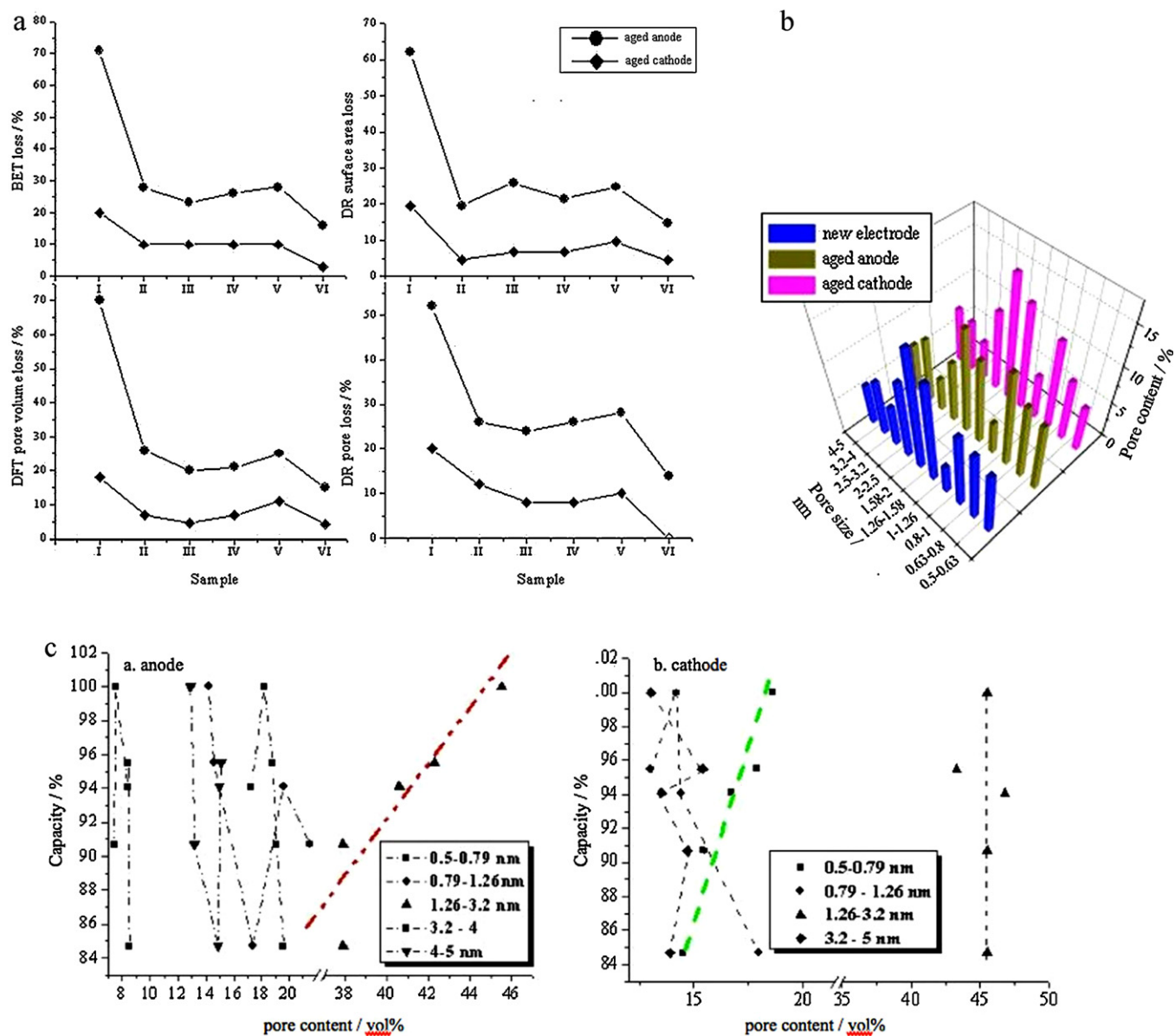
Fig. 3. (a) Comparison of loss of specific area (BET and DR) and pore volume loss (DFT, DR) for aged anodes and cathodes of samples I to VI (see Table 1). (b) Pore size distribution histogram (DFT): comparison of new and aged electrodes. (c) Relation of capacitance (measured by electrochemical impedance spectroscopy) and porosity (from b). The relation is linear only for pore sizes 1.26–3.2 nm (anodes) and 0.5–0.79 nm (cathodes).
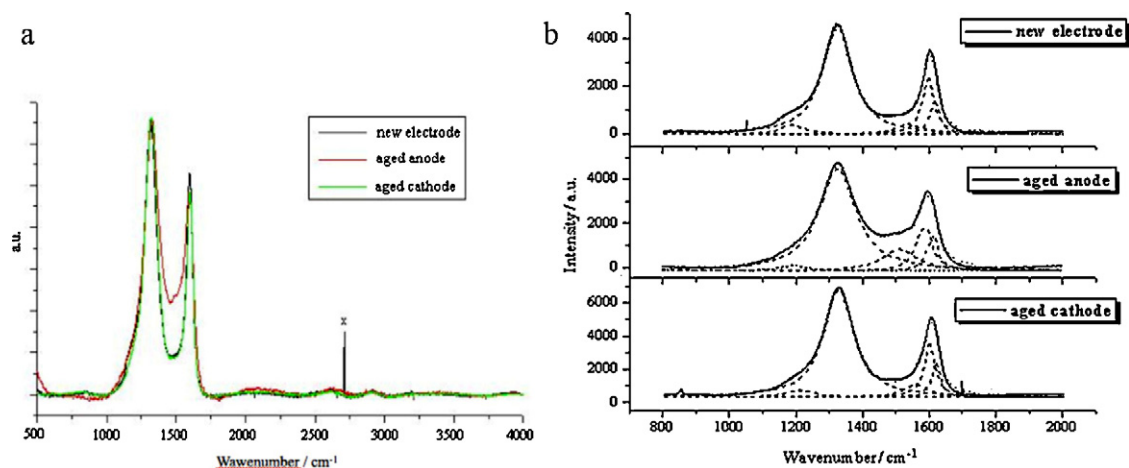

Fig. 4. (a) Raman spectra from new and aged electrodes. X marks an artifact. (b) Details and curve fitting for the D and G bands.

Table 3
Raman bands of samples and related carbon materials.

Sample	Raman bands[a]/cm^{-1} and intensities rel. to the G band				
	D$_1$ (D)	D$_2$ (D')	D$_3$ (D'', A)	D$_4$ (I)	G
New	1318, 4.8	1611	1534, 0.37	1185, 0.32	1591, 1
Anode	1324, 5.5	1610	1511, 1.06	1190, 0.21	1584, 1
Cathode	1321, 5.6	1613	1555, 0.50	1206, 0.28	1594, 1
Non-graphitizable	∼1350, >1	∼1620, ∼1	1500, <1	1200, ≪1	∼1580, 1
Disordered[b]	∼1350, <1	∼1620, ∼1	–	–	∼1580, 1
Ordered[c]	–	–	–	–	∼1580, 1
Band assignment	Disordered graphene edges (A$_{1g}$)	Disordered graphene surfaces (E$_{2g}$)	Amorphous carbon	Disordered; polyenes; ions (A$_{1g}$)	Ideal graphite (E$_{2g}$)

[a] Alternative band designations are given in brackets.
[b] Polycrystalline graphite (<100 nm) and boron-doped HOPG.
[c] Single crystalline graphite (>100 nm) and HOPG.

the G band. A simple interpretation is a lattice vibration analogous to that of the G band (E$_{2g}$ symmetry), but involving layers at the surface of a graphitic crystal, i.e. graphene layers that are not directly sandwiched between two other graphene layers. Indeed, D$_2$ was observed to replace G in intercalation compounds [26,27]. However, the D$_2$ band (and also D$_1$) results from a disorder-induced double resonance effect, and its origin is controversial [28–32]. Our Table 3 refers to earlier studies of various carbonaceous substances, which were summarized by Sadezky et al. [33]. At 1596 cm^{-1} we found the G band (E$_{2g}$ symmetry), which is the main band in crystalline graphite, and also the main structural element in AC.

Between G and D$_1$, the Raman intensity shows a minimum, a "valley" at ≈1500 cm^{-1}. Raman spectra from aged anodes show a higher "valley" than found in new electrodes and aged cathodes. This can be attributed to another band, which has been designated D$_3$ (Table 3). Its presence is linked to a statistical distribution of amorphous carbon on interstitial places in a disturbed graphitic lattice; in other words, it originates from the amorphous carbon fraction of carbon black or AC (organic molecules, or small fragments) [33–35]. The fraction of amorphous carbon in aged anodes is higher than in aged cathodes and new electrodes, which we attribute to more complex functional groups formed during the ageing. This fits well also to the chemical ageing (see below). The D$_1$ band at 1316 cm^{-1} is strong only for highly disordered graphitic structures. It corresponds to a graphitic lattice vibration mode of A$_{1g}$ symmetry, originating from the reduced symmetry near edges or heteroatoms. Moreover, this band has been observed in Raman spectra taken on the edge planes (perpendicular to the graphene layers) of large graphite single crystals, and of highly oriented pyrolytic graphite (HOPG). Thus, carbon atoms at the edges of graphene layers are considered as the most probable origin of the D$_1$ band in AC [32,36]. Certainly such atoms are prone also to chemical changes. After ageing, the intensity ratio $I(D_1)/I(G)$ increases, which means the disorder increases. Moreover, $I(D_3)/I(G)$ of anodes is much higher than that of new electrodes and aged cathodes. In passing we note that due to the resonance effect mentioned already for D$_2$, the location of D$_1$ depends on the excitation laser, and is 1350 cm^{-1} for the more common excitation at 514 nm [34,37,38].

A peak at 1200 cm^{-1}, designated as D$_4$, appears as a shoulder on D$_1$. Dippel et al. observed this band ≈1190 cm^{-1} in Raman spectra of flame carbon black, and tentatively attributed it to sp^2–sp^3 bonds, or C–C and C≡C stretching vibrations, as found in Raman

experiments with polyene-like structures [39,40]. Sadezky et al. [33] support the inclusion of a D$_4$ band with Lorentzian line shape at ≈1180 cm^{-1} in their work, and find that the intensity of this peak increases with the increase of excitation laser wavelength, which explains why this peak was not reported in earlier work performed with 514 nm excitation. For comparison, polyaromatic hydrocarbons (PAHs) such as hexabenzocoronene show a clear peak at 1250 cm^{-1} (excited at 633 nm), but no significant D$_3$ band, which is in good agreement with theoretical calculations [41]. From this result we infer the presence of "PAH-like" elements, which are in fact graphene planes of the size of a large molecule. Our results show that ageing decreases D$_4$ on anodes while there is no significant change on cathodes.

Our Raman results add important points to the porosimetry results. Given the rather inert chemical nature of AC and carbon black (and fluoropolymer binder), the observed increase in disorder can only be observed on long time scales (months), especially in aged anodes. The nature of this disorder is not clear: some parts of the structure, especially graphene edges and sp^3 atoms, are reactive and able to rearrange under electrochemical polarization. This is also true for "PAH-like" structures that appear to be converted to other species in anodes only. On the other hand, such processes should be linked to electrochemical reactions, and exactly under these conditions we observe also reactions of electrolyte species, as detailed in the following sections. In other words, we can observe structural changes, but the origin is based on electrochemical reactions.

3.3. Chemical ageing of electrodes

3.3.1. Elemental analysis and XPS

Different from pure activated carbon, which contains more than 90% carbon, the electrodes are composed of several ingredients, including carbon black and binder. Hence the carbon content is below 90% (see "ele" results in Table 4). As expected, there is little hydrogen. Striking is the increase of the nitrogen content on aged anodes, compared to new electrodes (below the detection limit of ≈0.1%), and to aged cathodes. Since the samples were washed carefully, nitrogen is not from adsorbed electrolyte (TEA$^+$ or acetonitrile); crosschecks with unrinsed samples showed that in this case the aged electrodes do not differ much in nitrogen content. Hence we propose that – similar to pure AC [15] – new nitrogen

Table 4
Concentration of elements in electrodes, obtained by elemental analysis ("ele") and by XPS.

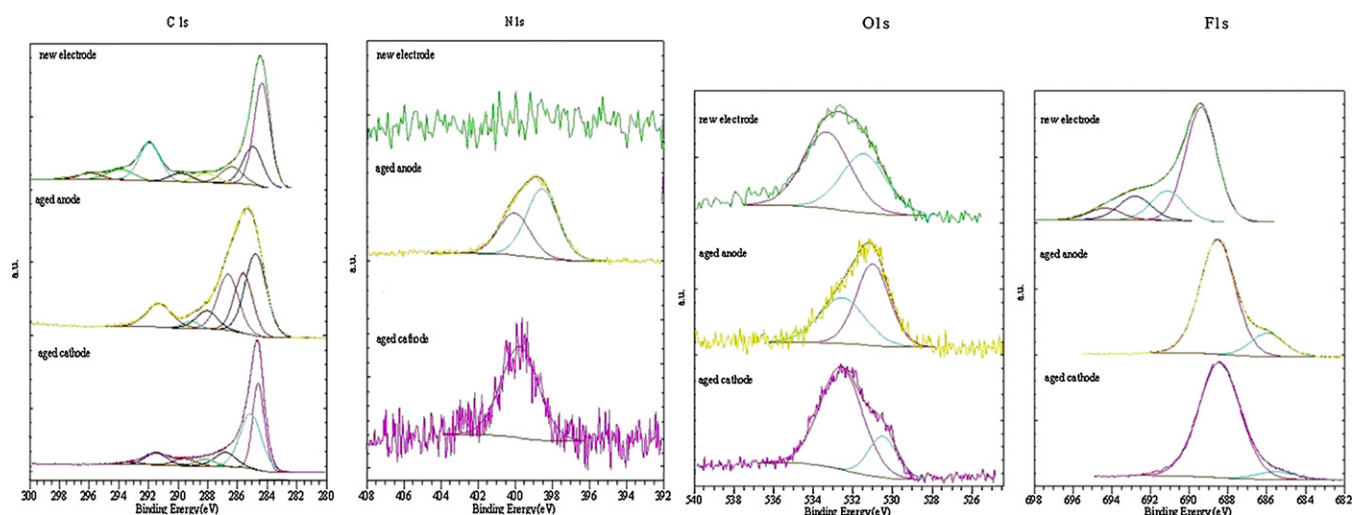| Sample	Atom % C (ele, XPS)	Atom % H (ele)	Atom % N (ele, XPS)	% others (ele)	Atom % F (XPS)	Atom % O (XPS)
New electrode	88.7, 63.6	0.4	0.0, 0.0	10.9	35	1.4
Aged anode	86.4, 64.5	0.8	1.5, 12.5	11.3	20.7	2.3
Aged cathode	89.5, 79.8	0.8	0.3, 0.0	9.4	17.7	2.5

Fig. 5. XPS spectra from new electrodes, and aged anodes and cathodes, for C1s, N1s, O1s, and F1s signals. The deconvolution into subpeaks is shown. Noisy spectra (N1s and O1s) point towards very small content of the respective element (see Table 4).

species form on anodes during ageing. The nitrogen content on the cathodes is low, but not zero, which is again comparable with the results from the pure AC [15], and also from other electrodes. A huge problem of the analysis is the presence of fluorine in the binder, which should be included in "others" (elements other than carbon, hydrogen, and nitrogen), but this is prone to errors since fluorine was not detected. Consequently, we employed XPS to obtain details. The relative elemental contents (except hydrogen) calculated from XPS overview spectra do not correlate well with the elemental analysis (see Table 4), as discussed above, but we deem the XPS data more reliable since fluorine is measured, too. The neglected content of hydrogen plays a minor role, as obvious from the elemental analysis. However, the decisive advantage of XPS is based on recording energy scans around elemental peaks (Fig. 5), which allow for a detailed analysis of the element's oxidation state. We note that most of the results are in line with recent investigations on pure activated carbon [15], capacitor electrodes [5,8,13], and other capacitors [2,6].

We were able to apply a deconvolution processing to the rather complex shape of the carbon C1s peak (Table 5). We found that the binding energy of each component of the peak varies slightly (±0.3 eV) from sample to sample, which is expected because of the large variation of local environment as the surface functionality changes. This phenomenon was also observed by Azaïs et al. [8]. From the data in the table, the ratio of graphitic carbon decreases after ageing in both anodes and cathodes. This indicates that the graphitic structure is partially broken during ageing, which nicely confirms our Raman results. These processes can occur on AC and on carbon black, which we do not distinguish in this section; they may additionally also have contributions from changes in the fluoropolymer binder.

In new electrodes, the graphitic peak component is largest. The absence of the peak at 289.3 eV and the rather small peak at 288 eV indicates that they contain quinones or other ketones, and ethers or hydroxyl, but few carboxyl groups ("carboxyl" denotes carboxylic acids and their derivatives, such as esters, amides, anhydrides). We readily detected the fluoropolymer carbon at 291.7 eV and 294.2 eV. Here and in the following, we compare our XPS data of carbon bound to heteroatoms with data from polymers [42–46] and from carbon fibers [47–50]. Note that a highly shifted signal (6.9 eV above the main C1s peak) was found to disappear whenever we expected a significant amount of functional groups. This signal can be explained as a plasmon satellite, which may appear when the photoelectrons escape from the surface and are subject to plasmon excitation (originating from periodic oscillations of charge density in conductive media) [48]. The peak at 296.2 eV was only found for new electrodes; its origin is unclear. Ageing produces a range of new subpeaks of C1s (Table 5, Fig. 5), which are discussed in detail in the following.

On the aged cathode we found very little nitrogen, so the deconvoluted C1s peaks are assigned exclusively to C–C, C–O, and C–F species (the latter stem exclusively from the binder). The peak at ≈285.2 eV can be assigned to C–H and C–C bonds at the edge of graphene sheets; the peak at ≈286.8 eV to ketones and quinoids, as well as ethers or hydroxyl. A new signal at 289.6 eV can be interpreted as carboxyls, but also as partially reduced fluoropolymer. The latter fits well to the reduced main signals from the fluoropolymer binder (291.5 and 294.2 eV). We conclude a partial cathodic hydrogenation of the binder, which is rather unusual, and certainly caused by the long-term polarization. The required hydrogen (and also oxygen) can stem from multiple sources: first, water and oxygen permeation is possible even into a well-sealed system after
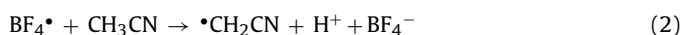
Table 5
Ratio (%) of various components of the XPS C1s signal in electrodes.

Peak	Binding energy/eV	Assignment	New electrode	Aged anode	Aged cathode
I	284.6	Graphite	48.7	34.3	33.0
II	285.5 ± 0.3	C–H, C–C at the edge of graphene sheets; C–N	11.8	21.7	38.0
III	286.8 ± 0.3	C=O in ketones; C–OH; C–O–C; C=N–C	5.2	22.8	9.6
IV	288.2 ± 0.3	C=O in ketones and carboxyls; C=N–C; CHF species	2.5	7.5	4.2
Va	289.3 ± 0.3	C=O in carboxyl; CHF species	0.0	2.0	4.8
Vb	290.2 ± 0.3	C=O in carboxyl; π–π^* transition	4.4	0.0	0.0
VI	291.7 ± 0.3	CF_2; plasmon	18.6	11.7	8.4
	294.2 ± 0.3	CF_3	6.0	0.0	2.0
	296.2 ± 0.3	–	2.8	0.0	0.0

long-term operation. Note that AN vapor and also some gases can leak out, as proven by the observation of the weight loss and gas evolution of EDLCs [11]. In this case, it is especially likely that water and oxygen from air can diffuse inside. Secondly, water might also be trapped in the pores of the activated carbon, in the separator and in the aluminum foil, and be difficult to remove completely during the drying step of the manufacturing processes [13]. Thirdly, there are various sources for protons: AN may act as a proton source; it is a very weak Bronsted acid, (pKa = 25), and also allows for autoion-ization:
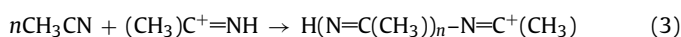
$$2CH_3CN \rightarrow CH_3CNH^+ + CH_2CN^- \tag{1}$$

Ethylene elimination [9] can produce protons even more effectively. However, the deprotonization can also be promoted by oxidation of TFB$^-$ to the TFB radical [51], which abstracts a proton from acetonitrile

$$BF_4{}^\bullet + CH_3CN \rightarrow {}^\bullet CH_2CN + H^+ + BF_4{}^- \tag{2}$$

Aged anodes show a very different behavior in the C1s signal. Here the intensities of peaks at ≈285.5 eV, 286.6 eV, and 288.2 eV increase markedly, compared to new samples, while the graphitic carbon signal at 284.6 eV decreases sharply. While most of these effects are based on C–O bonds (e.g. in carboxyls) formed by oxidation, the signal at 285.5 eV can here partially be due to C–N bonds (e.g. amines as in polymerized AN), as already postulated by Eggert and Heitbaum [12]. At 288.2 eV and 289.3 eV amides certainly contribute. The fluoropolymer binder (291.3 eV) concentration decreases; this phenomenon has been observed in the modification of fluoropolymer surfaces by plasma treatment [52–54], radiation grafting [55] or degradation [56–59]. On the other hand, the peaks at lower binding energies (289.0 eV, 288.0 eV) would then correspond to partially hydrogenated fluoropolymers, which are more likely present on cathodes.

The O1s signal shows much less structure. Aged anodes and cathodes exhibit two peaks at ≈533.0 eV and 531.2 eV (Fig. 5). Although these are close to those on the new electrode, the assignment should be different, as we infer from the C1s and IR results (see below). We intend to assign the peak at ≈533.0 eV to ethers and hydroxyl, while 531.2 eV is typical for ketones and carboxyls.

The N1s peak of the aged anode is the clearest indication for covalently bound nitrogen. Possible sources are the cation, but especially the AN. A well-known reaction is its (anodic) polymerization [60], which fits very well with our porosimetry data, and with the C1s components in anodes:

$$nCH_3CN + (CH_3)C^+{=}NH \rightarrow H(N{=}C(CH_3))_n{-}N{=}C^+(CH_3) \tag{3}$$

(this polymer can be attached to AC covalently or by van der Waals forces). The N1s peak is split into two components at 398.8 and 400.2 eV (Fig. 5). The first can be assigned to pyridine-like moieties (–C=N–C–), to amines, or to C=N as found in polyacetonitrile; the

second stems from amides. At 401–402 eV no signal for quaternary nitrogen is found, hence we exclude the presence of TEA$^+$. In passing we note that we also exclude high oxidation numbers such as in nitro groups since they would result in much higher shifts (above 405 eV) [61,62]. Although we found N1s signals also on aged cathodes, already the signal to noise ratio indicates that the nitrogen content is very low. In some cathode samples this peak disappeared altogether.

In the F1s spectrum of the new electrode we observed a strong peak at 689 eV, corresponding to the fluoropolymer, and three peaks at higher binding energies (Fig. 5). The latter cannot be correlated with groups like CH_nF_{2-n}, which are produced only by ageing, so they might point towards contamination during the electrode processing. These peaks, and also C1s signals of high chemical shifts disappear with ageing. The F1s peak of the aged electrodes both contain two chemical shifts: 688.8 eV, which can be assigned to CF$_2$ in the fluoropolymer (consistent with the C1s signal at ≈291.3 eV), and ≈686 eV, which might be due to partial hydrogenation of the fluoropolymer. As discussed above, this process is likely on cathodes, but not expected on anodes.

3.3.2. Infrared spectroscopy

IR spectra can give additional information (especially for hydrogen), or even replace the much slower and expensive XPS analysis, whenever a simple analysis is sufficient. Unfortunately, one frequently encounters problems in sample preparation, poor transmission, uneven light scattering related to large particle size, etc. [63]. Moreover, some band assignments differ substantially among the published IR studies on carbon materials. Fanning and Vannice analyzed data from earlier results, and tried to establish a consensus in assignments to various functional groups. Most data from later work is consistent with their summary [64]. Generally, signals from the "outer surface" of electrodes (the one exposed to the separator) was stronger than that from "inner surfaces", which we exposed by stripping off a part of the electrode with adhesive tape. Overview spectra in the range from 4000 to 700 cm^{-1} are shown in Fig. 6 and summarized in Tables 6 and 7. The effective penetration depth and thus absorption of IR in a conductive solid is stronger at low wavenumbers, so the overall shape of IR spectra of carbon is determined by a strong slope in the baseline, which is clearly visible in our spectra. We decided to avoid any baseline correction in order to avoid artifacts, hence we simply divided the single beam spectrum from each sample by that from the background (air) (standard IR "subtraction").

The detailed spectrum of the fresh electrode (Fig. 6) shows only three bands at 1580 cm^{-1}, 1220 cm^{-1}, and 1154 cm^{-1}. The latter can be assigned to the fluoropolymer binder in the electrode. The broad band at ≈1580 cm^{-1} is a prominent feature in the IR spectra of active carbons, chars, coals, etc. A simple assignment to vibrations of the basal plane of graphitic carbons does not suffice, it

Table 6
IR bands (cm^{-1}) and their assignments.

New electrode	Aged anodes	Aged cathodes	Assignment
–	3600–3000 br	3600–3000 br, w	N–H str., O–H str.
–	3100–2800 m	3100–2800 m	C–H str. C–N–H str., O–H str.
–	1750–1600 br	–	C=O str. (carboxyls), C=N str., amide I
1580 m	1580 m	1580 m	C=C str. (conjug.), C=O str.
–	1540 m	–	Amide II
–	1436 s	1420 w	C–O–H def., C–N–H def., C–H def., C=C str. (aromats)
–	1350 w	–	O–H def., C–N str., C–O str.
1220 s	1220 s	1220 s	C–F asym. str. in CF$_2$
1154 s	1154 s	1154 s	C–F sym. str. in CF$_2$
–	1110–1000 br	1110–1000 br,w	C–O str.
–	–	1000–800 br,w	C–H def.

s = strong; m = medium; w = weak; br = broad; str. = stretching; def. = deformation; asym. = asymmetric; sym. = symmetric.
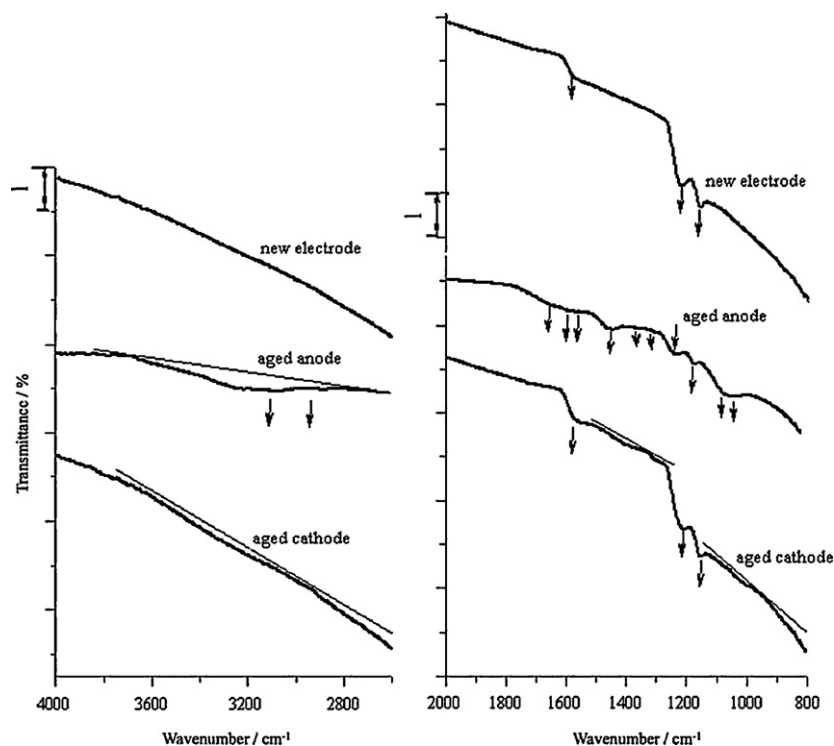
Fig. 6. Infrared spectra for new and aged samples in the spectral regions 4000–2600 cm^{-1} and 2000–800 cm^{-1}. Spectra are vertically shifted for clarity.

appears that functional groups have to be present [63–66]. Mostly, these are based on oxygen, and the C=O stretching modes from quinoids play a role [67,68]. Note that bands from solvent or electrolyte are absent. The same three bands can also be found on the aged anode and cathode, although their relative intensity is smaller. The more interesting signals are those that appear only by ageing: bands between 3600 and 3000 cm^{-1}, a broad band between 1750 and 1600 cm^{-1} (maximum at ≈1660 cm^{-1}), a strong band at 1436 cm^{-1}, a weak band at 1350 cm^{-1}, and a broad band between 1110 and 1000 cm^{-1}. We assigned them based on literature values [25,63,64].

At high wavenumbers we observe C–H, O–H, and N–H stretchings, which are a valuable add-on to elemental analysis and XPS results. Obviously, many of these signals stem from hydrogenation or hydration [11]. Since nitrogen species exist on aged anodes, the broad band between 3600 and 3000 cm^{-1} can be assigned to O–H or N–H stretching modes, while cathodes and new electrodes should feature only O–H. The bands ≈3600 to 3350 cm^{-1} are normally from free O–H stretching modes in phenolic or carboxylic acid structures; they can also be due to free N–H stretching modes from primary amide or amine groups. Bands in the lower range from 3400 to 3200 cm^{-1} can be assigned to associated O–H groups, or to N–H. C–H stretching modes are located in the region from 3100 to 2800 cm^{-1}, and are hard to distinguish from the former two bands [25,63], but present in cathodes. This points to reductive hydrogenation, as we already postulated from our XPS analysis.

In the range 1800–1600 cm^{-1}, we were unable to detect the C=O stretching mode from anhydrides (1800–1740 cm^{-1}), but

other carboxyls (acids and lactones from 1790 to 1660 cm^{-1}), ketones and quinoids (1700–1550 cm^{-1}), and the amide I band (1695–1630 cm^{-1}). C=N stretching modes show up at slightly lower frequencies, but are hard to distinguish. The intensities of these bands were much reduced for aged cathodes, which strongly supports our hypothesis of very slow anodic oxidation. The band at 1540 cm^{-1} can be interpreted as amide II band, and indeed we detected it only on (nitrogen-rich) aged anodes. The region of 1460–1400 cm^{-1} can be assigned to C–O–H bendings in carboxylic acids and phenols, but also to C–N–H bendings, C–H deformations, and even to aromatic C–C stretches. The bands at ≈1370 cm^{-1} and 1340 cm^{-1} (weak intensity) are considered to be from O–H deformation vibrations, or C–N stretching modes in amides, or C–O stretching modes in lactones. In the range of 1300–1000 cm^{-1}, we find one broad band and two maxima ≈1060 and 1035 cm^{-1}. While this would fit to some vibrations in the electrolyte salt, C–O stretches and N–H bendings are more likely. While all these signals cannot be clearly assigned, they fit nicely to our XPS results, and are easily distinguished from new electrodes. Finally, aged cathodes feature a broad and weak band from 1000 to 800 cm^{-1}, which might be due to C–H out-of-plane bendings.

3.4. Other components – aluminum foils, separator

Some of the postulated mechanisms correlate very well with results obtained for the other components of the capacitors. We did not characterize these components in depth, but we deem our results relevant. Note that the electrolyte, while mainly absorbed in

Table 7
Chemical species and functional groups in new and aged electrodes.

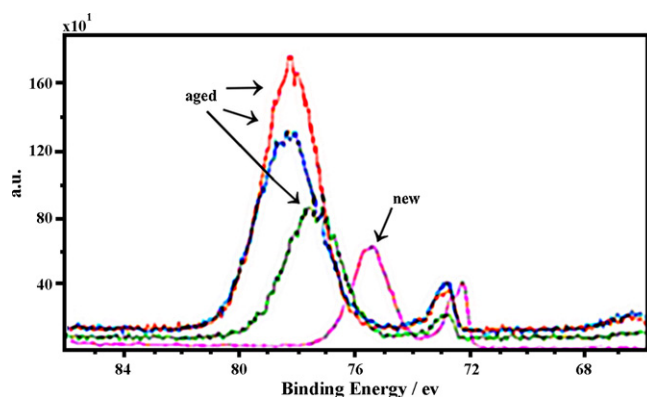| New electrodes	Aged anodes	Aged cathodes
Reactive C (edges, defects). Carboxyls, ketones, ethers. CF species.	Reactive C (edges, defects), C–H species. Carboxyls. Amides, amines (incl. polyacetonitrile), pyridinic structures. CF species (incl. CHF).	Reactive C (edges, defects), C–H species. Ketones, ethers, hydroxyls, carboxyls. CF species (incl. CHF).

Fig. 7. XPS of aluminum features (Al2p) in new and various aged aluminum foils.

the pores of the carbon electrodes, is in contact with the casing and the aluminum foil, which forms electrode support and electrical connection, and also with the paper separator. Harmful compounds can diffuse through the electrolyte and reach all parts of the capacitor. We found that ageing of the separator was the most obvious effect of all: the separator in the capacitors that were aged severely had always changed color from nearly white to deep yellow, or even to brown. This effect was especially pronounced for the side that touched the anode. Optical micrographs showed very dark inclusions, several μm in size. Fresh separators were completely soluble in concentrated H_2SO_4, a process based on protonation and probably also oxidation of lignins and cellulose. In contrast, the severely aged dark separators left a small amount of dark residue in H_2SO_4, which suggests the presence of carbon. We propose that water is eliminated from the paper, according to the simplified reaction:

$$(CHOH)_n \rightarrow nC + nH_2O \qquad (4)$$

The consequences of such a reaction, thermodynamically favored, but proceeding at very low rate, are severe, since it produces water and thus protons. Already Ishimoto et al. mention that water can indeed be produced inside capacitors by chemical reactions [13]. The separator might be a more effective source of protons than the Hofmann elimination from TEA$^+$ [9], or the deprotonation of acetonitrile (Eq. (1)). Note that protons could even diffuse to the cathode, and be reduced to hydrogen [11]. Already from these results we can suggest to consider not only the electrodes, but also carefully select the separator material to counteract ageing.

The XPS analysis of the aluminum foils (Fig. 7) revealed the expected elements, namely aluminum and oxygen, the latter due to the thin passivation layer. Fresh capacitors show the expected Al2p peaks at 72.5 eV (aluminum) and 75.5 eV (surface oxide). The high surface sensitivity of XPS explains why the oxide peak is stronger than the metal peak. After ageing, electrodes still show the metal peak (72.8 eV), but no signal at the oxide position, and a very strong peak at 78.2 eV, which is not compatible with other elements. Such a high shift can only be interpreted as AlF_3 or surface-fluorinated aluminum, as found be Strohmeier for aluminum annealed in the presence of NH_4BF_4 [69]. We interpret this as partial destruction of the passive layer according to

$$6HF + Al_2O_3 \rightarrow 2AlF_3 + 3H_2O \qquad (5)$$

as also reported by Chiba et al. [14], and similar to results by Kurzweil and Chwistek [9]. The existence of Al–F bonds verifies our assumptions about the presence of BF_4 radicals and/or HF, which is found in destroyed capacitors [9,14]. While the radicals can only be produced at the anode and react with it, HF can also diffuse through the electrolyte and reach any point inside the capacitor. The

presence of a layer that is at least several nm thick (thus suppressing the XPS signal from the pure aluminum; similar to SIMS [9] and EDX results [14]) means that adhesion and electrical contact to the carbon electrode are impeded. Indeed, in some cases the carbon peeled off very easily, and such a delamination could by decisive for the increase of the ESR. Obviously the process cannot be suppressed with glues based on carboxymethyl cellulose, although they are beneficial.

4. Conclusions

Multiple ageing mechanisms operate in EDLCs. While we detected ageing also for the aluminum and paper surfaces (casing and separator), we focused on the electrodes. As emerging also from other studies, aged anodes suffer more from ageing than aged cathodes. Specific area and pore volume of aged anodes are strongly affected. For the capacitance loss, pores in the size range from 1.26 to 3.2 nm are more important than the pores in other size ranges. Large micropores (1.26–2 nm) and small mesopores (2–3.2 nm) are blocked by polymerized solvent acetonitrile (AN). Aged anodes have a more disordered structure. Such a structural ageing is physical in nature, but caused by electrochemical processes, e.g. oxidation of the carbon. For cathodes, we attribute the smaller loss in capacitance to pores in the size range from 0.79 to 1.26 nm, blocked by the ageing products, which are again based on electrochemical reactions.

On new electrodes, only small amounts of oxygen species exist, but, together with the complex structure of the carbon, they allow for a certain reactivity that even extends to the fluoropolymer binder. On cathodes, the carbon is partially reduced, and some CH groups form. On anodes, it is oxidized, which incorporates nitrogen and oxygen in form of various chemical groups (see Table 7). The required hydrogen and oxygen may stem from water traces [13], but also from organic material such as the paper separator. All these effects are extremely slow, and cannot easily be traced to known reactions. Due to the small size of the pores, many chemical reactions are related to structural defects.

Since especially carboxyl species form, and since mainly the anode is affected, sources of oxygen should be avoided to prolong EDLC lifetimes. However, the formation of nitrogen-containing species from electrolyte and solvent decomposition cannot be avoided. The electrolyte may also produce the reactive BF_4 radical, and fluorinations and HF formation become possible. This would explain the formation of Al–F bonds on the aluminum electrode support, which can cause at least local delamination of the carbon electrode, and thus increase the equivalent series resistance (ESR).

Appendix A. Supplementary data

Supplementary data associated with this article can be found, in the online version, at doi:10.1016/j.jpowsour.2011.10.083.

References

[1] A. Burke, Int. J. Energy Res. 34 (2010) 133–151.
[2] R. Kötz, P.W. Ruch, D. Cericola, J. Power Sources 195 (2010) 923–928.

[3] D.M. Steiner, M. Klohr, S. Pagiela, European Conference on Power Electronics and Applications, vol. 1–10, 2007 Aalborg, 2007, pp. 982–991.
[4] A.G. Pandolfo, A.F. Hollenkamp, J. Power Sources 157 (2006) 11–27.
[5] P.W. Ruch, D. Cericola, A. Foelske-Schmitz, R. Kötz, A. Wokaun, Electrochim. Acta 55 (2010) 4412.
[6] P.W. Ruch, D. Cericola, A. Foelske, et al., Electrochim. Acta 55 (2010) 2352–2357.
[7] E. El Brouji, J.M. Vinassa, O. Briat, N. Bertrand, J.Y. Deletage, E. Woirgard, IEEE Energy Conversion Congress and Exposition 1–6 (2009) 1718–1725.
[8] P. Azaïs, L. Duclaux, P. Florian, D. Massiot, M.-A. Lillo-Rodenas, A. Linares-Solano, J.-P. Peres, C. Jehoulet, F. Bégiun, J. Power Sources 171 (2007) 1046–1053.
[9] P. Kurzweil, M. Chwistek, J. Power Sources 176 (2008) 555–567.
[10] R. Kötz, M. Hahn, R. Gallay, J. Power Sources 154 (2006) 550–555.
[11] M. Hahn, A. Würsig, R. Gallay, P. Novák, R. Kötz, Electrochem. Commun. 7 (2005) 925–930.
[12] G. Eggert, J. Heitbaum, Electrochim. Acta 31 (1986) 1443–1448.
[13] S. Ishimoto, Y. Asakawa, M. Shinya, K. Naoi, J. Electrochem. Soc. 156 (2009) A563.
[14] K. Chiba, T. Ueda, Y. Yamaguchi, Y. Oki, F. Shimodate, K. Naoi, J. Electrochem. Soc. 158 (2011) A872.
[15] M. Zhu, C.J. Weber, Y. Yang, M. Konuma, U. Starke, K. Kern, A.M. Bittner, Carbon 46 (2008) 1829–1840.
[16] J.F. Byrne, H. Marsh, in: J.W. Patrick (Ed.), Porosity in Carbons: Characterisation and Applications, Arnold, London, 1995, p. 1.
[17] O. Beyssac, B. Goffé, J.P. Petitet, E. Froigneux, M. Moreau, J.N. Rouzaud, Spectrochim. Acta Part A 59 (2003) 2267.
[18] M. Zhu, Ageing of Porous Carbon Electrodes, PhD thesis, EPF Lausanne, 2006.
[19] S.I. Lee, K. Saito, K. Kanehashi, M. Hatakeyama, S. Mitani, S.H. Yoon, Y. Korai, I. Mochida, Carbon 44 (2006) 2578.
[20] D. Qu, H. Shi, J. Power Sources 74 (1998) 99.
[21] J. Jagiello, C.O. Ania, J.B. Parra, et al., Carbon 45 (2007) 1066–1071.
[22] Y.J. Kim, Y. Horie, S. Ozaki, Y. Matsuzawa, H. Suezaki, C. Kim, N. Miyashita, M. Endo, Carbon 42 (2004) 1491–1500.
[23] M. Ue, K. Ida, S. Mori, J. Electrochem. Soc. 141 (1994) 2989.
[24] M. Endo, Y.J. Kim, H. Ohta, K. Ishii, T. Inoue, T. Hayashi, Y. Nishimura, T. Maeda, M.S. Dresselhaus, Carbon 40 (2002) 2613.
[25] D. Lin-Vien, N.B. Colthup, W.G. Fateley, J.G. Grasselli, The Handbook of Infrared and Raman Characteristic Frequencies of Organic Molecules, Academic Press, 1991.
[26] M.S. Dresselhaus, S.G. Dresselhaus, Adv. Phys. 30 (1981) 290.
[27] M.S. Dresselhaus, S.G. Dresselhaus, Topics in Applied Physics, vol. 51, Springer-Verlag, Berlin, 1982, p. 3.
[28] M.J. Matthews, M.A. Pimenta, G. Dresselhaus, M.S. Dresselhaus, M. Endo, Phys. Rev. B 59 (1999) R6585.
[29] C. Thomsen, S. Reich, Phys. Rev. Lett. 8 (2000) 5214.
[30] P.P. Vidano, D.B. Fischbach, L.J. Willis, T.M. Loehr, Solid State Commun. 39 (1981) 341.
[31] A.V. Baranov, A.N. Bekhterev, Y.S. Bobovich, V.I. Petrov, Opt. Spectrosc. (USSR) 62 (1987) 613.
[32] G. Katagiri, H. Ishida, A. Ishitani, Carbon 26 (1988) 565.
[33] A. Sadezky, H. Muckenhuber, H. Grothe, R. Niessner, U. Poeschl, Carbon 43 (2005) 1731.
[34] A. Cuesta, P. Dhamelincourt, J. Laureyns, A. Martinez-Alonso, J.M.D. Tscon, Carbon 32 (1994) 1523.
[35] T. Jawhari, A. Roid, J. Casado, Carbon 33 (1995) 1561.
[36] Y. Wang, D.C. Aolsmeyer, R.L. McCreery, Chem. Mater. 2 (1990) 557.
[37] S.K. Sze, N. Siddique, J.J. Sloan, R. Escribano, Atmos. Environ. 35 (2001) 561.
[38] R.L. Garrell, T.M. Herne, C.A. Szafranski, F. Diederich, F. Ettl, R.L. Whetten, J. Am. Chem. Soc. 113 (1991) 6302.
[39] B. Dippel, H. Jander, J. Heintzenberg, Phys. Chem. Chem. Phys. 1 (1999) 4707.
[40] H. Ishida, H. Fukuda, G. Katagiri, A. Ishitani, Appl. Spectrosc. 40 (1986) 32.
[41] C. Mapelli, C. Castiglioni, E. Meroni, G. Zerbi, J. Mol. Struct. 480–481 (1999) 615.
[42] D.T. Clark, Macromol. Chem. R. M. C. C. 12 (1975) 191.
[43] D.T. Clark, H.R. Thomas, J. Polym. Sci., Polym. Chem. 14 (1976) 1671.
[44] D.T. Clark, Phys. Scripta 16 (1977) 307.
[45] D.T. Clark, J. Polym. Sci., Polym. Chem. 16 (1978) 791.
[46] D.T. Clark, A. Dilks, J. Polym. Sci., Polym. Chem. 17 (1979) 957.
[47] A. Proctor, P.M.A. Sherwood, J. Electron Spectrosc. 27 (1982) 39–56.
[48] C. Kozlowski, P.M.A. Sherwood, J. Chem. Soc., Faraday Trans. 1 80 (1984) 2099.
[49] C. Kozlowski, P.M.A. Sherwood, J. Chem. Soc., Faraday Trans. 1 81 (1985) 2745.
[50] C. Kozlowski, P.M.A. Sherwood, Carbon 25 (1987) 751.
[51] G. Tourillon, P.C. Lacaze, J.E. Dubois, J. Electroanal. Chem. 100 (1979) 247.
[52] R.K.Y. Fu, Y.F. Mei, G.J. Wan, G.G. Siu, P.K. Chu, Y.X. Huang, X.B. Tian, S.Q. Yang, J.Y. Chen, Surf. Sci. 573 (2004) 426.
[53] U. Koenig, M. Nitschke, M. Pilz, F. Simon, C. Arnhold, C. Werner, Colloids Surf. B 25 (2002) 313.
[54] D.J. Wilson, R.L. Williams, R.C. Pond, Surf. Interface Anal. 31 (2001) 385.
[55] E. Adem, M. Avalos-Borja, E. Bucio, G. Burillo, F.F. Castillon, L. Cota, Nucl. Instrum. Methods B 234 (2005) 471.
[56] G.B. Hoflund, M.L. Everett, J. Phys. Chem. B 108 (2004) 15721.
[57] M.L. Everett, G.B. Hoflund, J. Polym. Sci. A: Polym. Chem. 43 (2005) 552.
[58] M.L. Everett, G.B. Hoflund, J. Phys. Chem. B 109 (2005) 16676.
[59] C.D. Li, D.Z. Yang, S.Y. He, Nucl. Instrum. Methods B 234 (2005) 249.
[60] P. Krtil, L. Kavan, P. Novák, J. Electrochem. Soc. 140 (1993) 3390.
[61] F. Kapteijn, J.A. Moulijn, S. Matzner, H.P. Boehm, Carbon 37 (1999) 1143.
[62] J. Lahaye, G. Nanse, A. Bagreev, Strelko, Carbon 37 (1999) 585.
[63] G. Socrates, Infrared Characteristic Group Frequencies, 3rd ed., Wiley & Sons, Chichester, England, 2000.
[64] P.E. Fanning, M.A. Vannice, Carbon 31 (1993) 721.
[65] A. Georgakopoulos, A. Iordanidis, V. Kapina, Energy Sources 25 (2003) 995.
[66] E. Fuente, J.A. Menéndez, M.A. Díez, D. Suárez, M.A. Montes-Morán, J. Phys. Chem. B 107 (2003) 6350.
[67] S. Biniak, G. Szymanski, J. Siedlewski, A. Swiatkowski, Carbon 35 (1997) 1799.
[68] J.L. Figueiredo, M.F.R. Periera, M.M.A. Freitas, Carbon 37 (1999) 1379.
[69] B.R. Strohmeier, Appl. Surf. Sci. 40 (1989) 249.